Journal of Biomedical Optics

BiomedicalOptics.SPIEDigitalLibrary.org

Toward an automated method for optical coherence tomography characterization

Mathias Strupler
Amber M. Beckley
Fouzi Benboujja
Sylvain Dubois
Isabelle Noiseux
Ozzy Mermut
Jean-Pierre Bouchard
Caroline Boudoux

SPIE.

Toward an automated method for optical coherence tomography characterization

Mathias Strupler,[a,*] Amber M. Beckley,[a] Fouzi Benboujja,[a] Sylvain Dubois,[b] Isabelle Noiseux,[b] Ozzy Mermut,[b] Jean-Pierre Bouchard,[b] and Caroline Boudoux[a]
[a]École Polytechnique de Montréal, Department of Engineering Physics, 6079 succursale Centre-ville, Montréal, Quebec H3C 3A7, Canada
[b]Institut National d'Optique, 2740 Einstein Street, Ville de Québec, Quebec G1P 4S4, Canada

Abstract. With the increasing use of optical coherence tomography (OCT) in biomedical applications, robust yet simple methods for calibrating and benchmarking a system are needed. We present here a procedure based on a calibration object complemented with an algorithm that analyzes three-dimensional OCT datasets to retrieve key characteristics of an OCT system. The calibration object combines state-of-the-art tissue phantom material with a diamond-turned aluminum multisegment mirror. This method is capable of determining rapidly volumetric field-of-view, axial resolution, and image curvature. Moreover, as the phantom material mimics biological tissue, the system's signal and noise levels can be evaluated in conditions close to biological experiments. We believe this method could improve OCT quantitative data analysis and help OCT data comparison for longitudinal or multicenter studies. [DOI: 10.1117/1.JBO.20.12.126007]

Keywords: optical coherence tomography; metrology; calibration; tissue phantom.

Paper 150569R received Aug. 24, 2015; accepted for publication Nov. 5, 2015; published online Dec. 17, 2015.

1 Motivation

Since its demonstration in 1990[1] and the subsequent implementation of Fourier domain techniques,[2] optical coherence tomography (OCT) has become an important diagnostic instrument in ophthalmology[3] and cardiology[4] as well as a promising tool in other clinical fields.[5] OCT provides cross-sectional images of semitransparent samples using low coherence interferometry, which can be implemented with a variety of illumination and detection schemes over a broad range of wavelengths and using multiple scanning geometries. This leads to a wide array of academic and commercial implementations of OCT, which in turns calls for better industry-wide system benchmarking.[6] Moreover, the trend toward extraction of quantitative data from OCT images (geometric features, attenuation coefficients, image feature extraction, etc.) vouches for a better calibration of OCT systems to improve reproducibility. Finally, it is crucial for longitudinal or multicenter studies to be able to perform system-to-system comparison and ensure that comparable measurements are taken in similar clinical conditions or as a system continues to be used over time.

In specifying OCT system performances, there are several attributes one can inspect: physical dimension of the acquired volume—or field-of-view (FOV), image curvature, resolution, sensitivity, signal-to-noise ratio (SNR), signal fall-off, vignetting, etc. These metrics are typically evaluated using planar objects such as mirrors, calibration targets, or metallic grids. In order to calibrate the OCT volume, it is necessary to axially move these planar objects with controlled steps. Moreover, several targets may be required to completely characterize an OCT system. Indeed, performing all these measurements on a single OCT system, using targets designed for *en face* imaging, is time-consuming, especially as no algorithm currently exists to automatically extract OCT characteristics from the acquired data. Hence, the complete characterization of a given system is rarely routinely performed, nor is the characterization method standardized between centers.

In this work, this issue is addressed by providing the OCT community with a simplified calibration and benchmarking procedure. Our vision is to combine a three-dimensional (3-D) calibration object with an algorithm able to automatically retrieve key parameters of the analyzed system. Complete characterization of a system should be performed rapidly and with a small number of operations. The availability of such a calibration procedure would allow an operator to calibrate his system as often as required and greatly enhance the reproducibility of the acquired data.

OCT is a cross-sectional imaging technique with a resolution on the order of a few microns. An ideal calibration object should therefore include micron-scale structures while being semitransparent to allow characterization of the system's depth imaging capability. Although OCT deals with high resolution, another challenge lies in the typical dimensions of the imaged volume. This can vary widely from system to system. For benchtop systems with Cartesian image geometry, it can be as large as a few centimeters in all axes. The calibration object needs to be larger than this but still contain micrometrics features.

Proposed solutions for such a calibration object include micron-scale lines engraved by femtosecond lasers in silica,[7] which test resolution, sensitivity, and distortion. Targets with variable size structures[8] were also demonstrated. They are meant to be a parallel for OCT to the US Air Force targets (Military Standard, Photographic Lenses, MIL-STD-150A)

*Address all correspondence to: Mathias Strupler, E-mail: mathias.strupler@polymtl.ca

used to calibrate *en face* imaging systems such as microscopes. Curatolo et al.[9] have presented a 3-D mesoscopic scale tissue phantom to provide a 3-D resolution target, with the size scales targeting typical OCT system performance. Similarly, there has been ongoing work to find appropriate phantoms for interlaboratory comparison or clinical benchmarking.[6,10,11] These calibration objects allowed for precise measurement of many OCT features, but none were accompanied by automatic analysis software.

Here, we present an OCT calibration method capable of measuring from a single 3-D acquisition: axial resolution, true volume dimensions, and image curvature. Our current approach is targeted to benchtop systems with Cartesian geometry and is based on a calibration object that combines the advantages of a tissue phantom with a precisely machined 3-D shape. In addition, a program automatically analyzes the data generated by the 3-D acquisition to benchmark and calibrate the OCT system.

2 Materials and Methods

This section describes the calibration object composed of a high-precision aluminum well and a tissue phantom, as well as the automated method to extract characterization metrics.

2.1 *Calibration Object*

Figure 1 shows a diagram of the cross-section of the circular calibration object, which combines two distinct technologies: single-point diamond turning to create surfaces with optical precision and a polyurethane-titanium dioxide solid setting liquid used as tissue-mimicking phantom material. The base is composed of a 2-in. diameter and ~1-in. high cylinder made of aluminum: an inexpensive, stable material easily machined to optical quality surface roughness. A well is machined on top of the cylinder, which is then filled with an imaging phantom material developed to mimic biological tissues.

2.1.1 *Aluminum well fabrication*

The aluminum cylinder, which forms the base, was machined into a well using single-point diamond-turning on a Nanotech 250UPL diamond-turning lathe (Moore Nanotechnology Systems, Keene, New Hampshire). With the ability to create large optical free-form surfaces in a reasonable time frame with a shape precision better than 1 μm, diamond-turning has the ability to create high quality and durable calibration objects. The 0.1 μm accuracy of this lathe is more than adequate for the creation of calibration objects for the OCT systems.

The circular symmetry of the lathe is exploited to create mirror rings as the machine cuts along one linear axis during the rotation of the metal base. The well base is composed of concentric rings of 1.000-mm wide mirror surfaces, each ring descending by 100.0 microns toward the center. In order to ensure a smooth machining process, 0.800-mm wide sloping transition zones between the flat rings were included in the design. Ten steps were cut, for a total well depth from top to bottom of 1.000 mm. The surface was cut by a single diamond tool (K&Y Diamond, Montreal, Canada) having a radius of curvature of 0.536 mm. Fifty machining steps using 25-micron deep cuts were necessary to create the well. The final surface was produced by performing a last 2.5-micron cut with mineral spirits spray for lubrication, a feed rate of 5 mm/min, and a spindle speed of 2000 rotation/min. Figure 2(a) shows the base after machining before being filled with the phantom material. Measurements of the well with an optical profilometer (Micromesure, STIL SA, France) show that the actual axial and lateral positions of the step edges vary less than 0.3% from the specified values and that each mirror plateau has a flatness better than 200 nm.

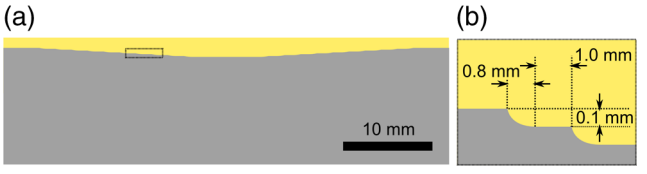

Fig. 1 Cross-section of the calibration object. (a) The cross-section of the target, with the well cut into the top of an aluminum cylinder, which is then filled with a tissue-mimicking material. A close-up of the rectangular region can be found in (b), where the step profile is described.

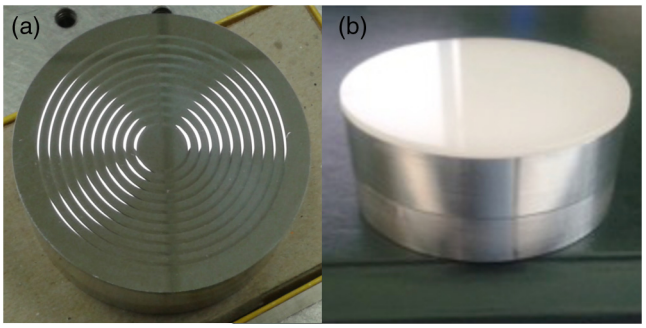

Fig. 2 The calibration object (a) before and (b) after being filled with phantom material. In (b), after it has been filled with phantom material, the top surface was machined to produce a smooth, flat interface parallel to the object bottom surface.

2.1.2 *Tissue phantom layer*

A uniform tissue phantom layer was added on top of the aluminium well. The material is a polyurethane polymer mixed with TiO_2 nanoparticles called biomimic, produced and provided by Institut National d'Optique, Canada.[10] This material was engineered to have stable and uniform optical characteristics (refractive index, absorption, and scattering).[12] The phantom's absorption and scattering coefficients at 750 nm are 0.097 and 9.55 cm^{-1}, respectively. The refractive index of the phantom material measured through ellipsometry at 1300 nm is 1.48 ± 0.02.

The well formed by the mirror plateaus was filled by phantom material in liquid form. The material was then allowed to solidify and adhere directly to the metal surface. The top surface was machined flat in order to remove imperfections and ripples in the solidified gel. Machining both the aluminum well and the phantom on the same lathe and using the back side of the aluminum well as a reference plane allows the mirror plateaus and the phantom surface to be parallel. The calibration target and phantom combination are shown in Fig. 2. Strong specular reflections attest to the low roughness of the first surface. The phantom material thickness is approximately 1.2 mm over the shallowest mirror segment and 2.2 mm over the deepest mirror segment, which is approximately scaled to the OCT imaging depth in biological samples.

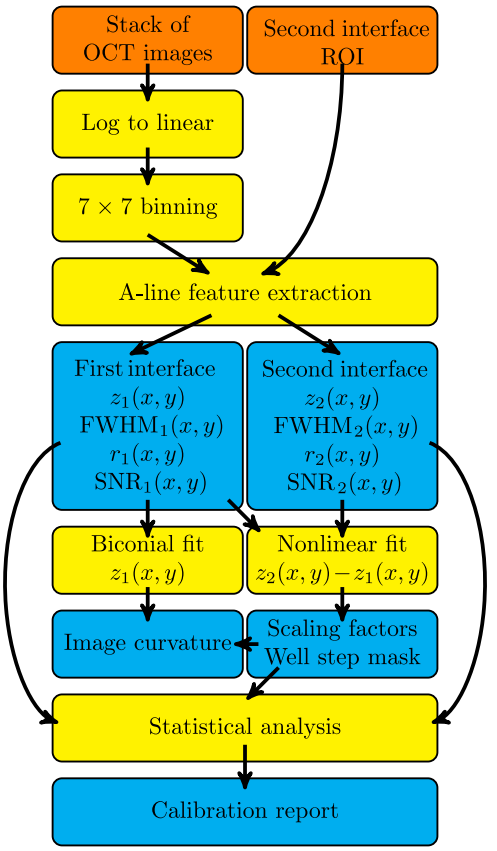

Fig. 3 Automated optical coherence tomography (OCT) benchmarking algorithm. Orange, yellow, and blue boxes represent the inputs, processing steps, and outputs, respectively.

2.2 *Automatic Analysis*

The algorithm that was developed for the automatic analysis as well as a calibration data set is discussed in Ref. 13,14. The software was written using Python, and the main algorithm steps are given in Fig. 3.

For input, the algorithm uses a stack of B-scans of the calibration object plotted in dB and saved as individual 8-bit grayscale image files. When acquiring and saving a stack of B-scans, the user should set the acquisition parameters and image dynamic range to maximize the 8-bit scale use while preventing saturation and setting the noise floor above zero in the 8-bit image scale. The imaged area should encompass a maximum number of well plateaus, including the deepest one. The sampling pitch in all dimensions should be better than 10 μm, and the image volume should be larger than 8 mm × 8 mm laterally and 3.5 mm axially. An example of such a dataset is presented in Fig. 4. In addition to the OCT images, the user must manually select the region of interest (ROI) where the steps of the well are located [see Fig. 4(b)] as well as the corresponding dynamic range in decibel.

All operations described henceforth are performed automatically. The first operation converts each A-line back to a linear scale and bins 49 adjacent A-lines (seven consecutive A-lines from seven consecutive B-scans) to improve the SNR. Each binned A-line is then analyzed to measure the properties (intensity and coordinates) of two reflectivity peaks related to the air-phantom interface and the phantom-aluminum interface. Detection of each interface is performed by finding the maximum reflectivity inside and outside the ROIs defined by the user [see Fig. 4(c)].

For each peak, the algorithm records its axial position, its full width at half maximum (FWHM), and its SNR, defined as the ratio between the peak amplitude and the noise standard deviation. To calculate the noise floor and its standard deviation, a portion of the binned A-line where no reflectors are present is used. This region is located just after the second interface (metallic) and is one-tenth of the A-line long. We also fit the attenuation length and amplitude of the signal from the phantom between both interfaces. This fit is used to calculate the signal-to-background ratio (SBR) for each interface—the amplitude ratio between the interface reflection and the phantom signal. An example of extracted features for the two surfaces is shown in Fig. 5. At this point, all coordinates are measured in pixel units.

In the next operation, the position of the second surface is subtracted from the position of the first surface to obtain a two-dimensional (2-D) map of the phantom thickness. Using the phantom thickness instead of the second interface coordinate directly removes most of the distortion and tilt and allows fitting of the theoretical well shape more easily. This fit uses six degrees of freedom: three for position and three for scaling. After completion, the scale factors that minimize the fit error give the pixel-to-micron conversion factor for each dimension. At this point, all pixel measurements can be transformed into physical distances. Moreover, the knowledge of the object position allows creating ROIs specific to each well step, as

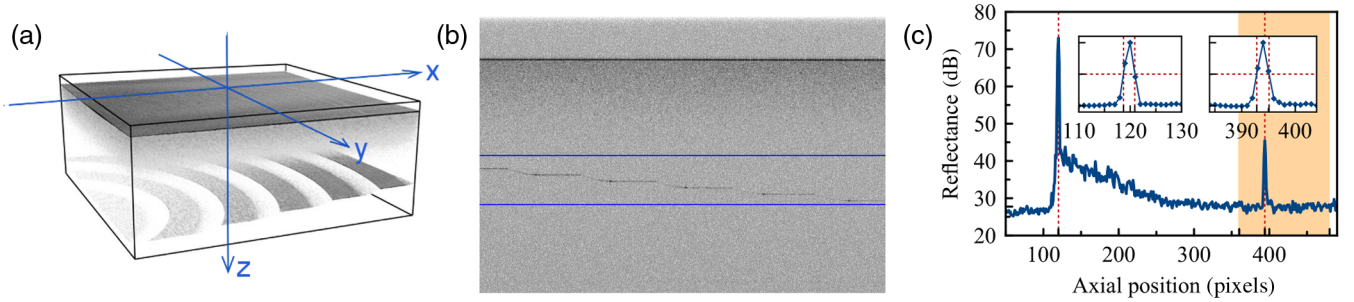

Fig. 4 (a) Three-dimensional view of a C-scan of the calibration object (1075 × 1075 A-lines)—fast (x), slow (y), and optical (z) axes shown in blue. (b) Typical B-scan showing the limits of the user-selected region of interest (ROI) (solid blue lines) encompassing the second interface. (c) Typical A-line (after binning) showing interfaces detected by the algorithm (dashed red lines). Orange-highlighted area corresponds to the user-selected ROI. Insets show normalized reflectance for each interface in linear scale, used to automatically compute the full width at half maximum (FWHM)—dashed red lines.

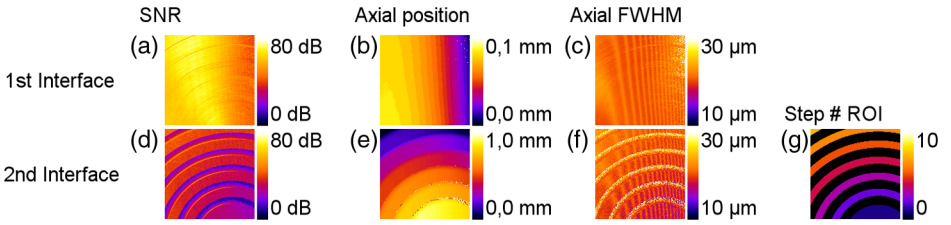

Fig. 5 *En face* views and corresponding lookup table showing the parameters extracted from each set of averaged A-lines. (a)–(c) show features related to the first (air-phantom) interface, whereas (d)–(g) are related to the second (phantom-aluminum) interface: (a) and (d) signal-to-noise ratio, (b) and (e) axial position, (c) and (f) axial FWHM, and (g) computed ROIs used to calculate the system properties at each mirror step.

represented in Fig. 5(g). In each ROI, the algorithm extracted statistics for: mean, median, minimum and maximum signal; standard deviation of its axial position; axial response FWHM; and SNR. The FWHM of the axial response was calculated only for points where both SNR and SBR were higher than 10 to avoid artificial broadening of the axial response. Finally, a fit of the first-interface coordinate image with a biconic function was performed to assess the *en face* OCT image curvature.

2.3 *Optical Coherence Tomography System Benchmarking*

The proposed method was applied to a commercial OCT system whose specifications are listed in Table 1. The calibration object was placed under the OCT objective lens so as to maximize the number of mirror segments—including the bottom of the well—visible within the image FOV. An OCT volume was acquired and exported as a stack of 2-D cross-sectional images. After opening the 3-D stack with an image stack viewer such as Fiji,[15] the ROI where the well steps were located was defined. The ROI selection is performed by looking at the whole 3-D scan, considering some mirror steps may not be visible in every frame. This ROI, along with the directory of the image stack and the dB range of the acquisition (the absolute values of the range limit are not necessary, only the range), were fed to the calibration software. The software automatically saves calibration results (images and text report). The whole procedure takes less than 10 min from placing the calibration object to generating the report. From those 10 min, only 2 min are used to run the algorithm on a conventional office computer.

Table 1 Optical coherence tomography system specifications

Parameter	Value
Central wavelength	1300 nm
Spectral bandwidth	~70 nm at −3 dB >100 nm at −20 dB
Coherence length	>100 mm
Sensitivity	100 dB
A-line rate	100 kHz
Max lateral field-of-view (FOV)	12 × 12 mm
Imaging depth (axial FOV)	12 mm
Axial resolution in air (FWHM)	16 μm
Lateral resolution	25 μm

3 Results

The procedure was repeated five times to assess the robustness of the algorithm and measure the errors on the output values. All acquisition parameters were kept the same for every procedure. The only change between the procedures was the position of the calibration object. Tests 1, 2, and 3 were performed with the calibration object at the same axial position along the optical axis of the OCT system but at different lateral positions. Tests 3, 4, and 5 were performed with the calibration object at the same lateral position but at different axial positions.

Figure 5 shows *en face* views of OCT features extracted during Test 1. All features were extracted correctly on the whole surface except for a few points for which the reflectance was too low to provide correct measurements. These erroneous points are mainly located in the curved transition section between adjacent mirror segments. Indeed, the slope in these sections reflects most of the beam energy away from the objective collection cone.

Figures 5(a) and 5(d) represent the SNR of the two interfaces. As seen in Fig. 5(d), SNR decreases as the mirror segment is buried deeper under the phantom material. The lateral position dependence of the reflected signal (within the same depth) is also noticeable. In test 1, the first interface of the SNR variation is as high as 30 dB (>95% of the reflectivity values are within this range).

The axial position for each of the two interfaces is depicted in Figs. 5(b) and 5(f). For the first interface, which is flat, tilt and curvature can be seen due to a combination of object tilt and system distortion, respectively. The discretization of the axial position can also be observed, as the calibration algorithm uses a simple maximum intensity search for this analysis. For the second interface, seven mirror segments are visible, each delimited by a 100-μm deep step.

Figures 5(c) and 5(g) show the FWHM of the axial response. What looks like an oscillating pattern is due to an arbitrary toggle between two values originating from the discretization of the OCT signal. On the left-hand side of Fig. 5(c), the lower reflected signal results in an increase of the FWHM. This is due to the fact that the SBR of those points falling below 10 affects the FWHM measurement. The algorithm removes such A-lines before calculating the FWHM value for the first

interface. The resulting precision is sufficient for most OCT system calibration.

From the extracted features, system benchmarks were obtained for each test and are summarized in Fig. 6. Relative positions of the calibration object with respect to the OCT system imaging FOV are presented in Figs. 6(a) and 6(b). For each experiment, an *x*-mark indicates the extracted position of the center of the calibrating object (i.e., the geometrical center of the deepest well) and is labeled with the experiment's number. As expected, the measured axial position of tests 1, 2, and 3 is identical [Fig. 6(b)], as the object was not moving axially during these tests. The measured position for tests 3, 4, and 5 is collocated laterally [Fig. 6(a)]. This is consistent with the absence of lateral movement of the object during between these tests. It can also be noted that the calibration object was moved more than 1 cm laterally and 2 mm axially to test the method robustness.

3.1 *Geometric Calibration*

An OCT acquisition can be seen as a collection of reflectance measurements taken at different positions in 3-D in a sample. The knowledge of the position of these samples is necessary to form an image or to do any geometrical measurement. In many cases, it is assumed that the sample points follow a rectangular grid with a constant spacing in any given direction. In practical implementations, this is never the case. For example, the OCT system used for this study relies on two dual-axis galvanometer mounted mirrors to scan the beam over the sample. As illustrated in Fig. 7, in a perfect image-space telecentric system, every output beam is parallel to the optical axis. In such a case, the OCT data geometry matches the Cartesian geometry of the reference frame of the laboratory. However, when the pupil position is not exactly placed at the back focal plane of the objective lens, OCT data are acquired with a spherical geometry. In the case of dual-axis galvanometer systems, only one scanning mirror can be placed at the objective pupil position. Hence, these systems cannot be telecentric in both dimensions. Nonlinear beam scanning, pupil aberration, and propagation in a nonhomogeneous medium can also alter the OCT data geometry. It is therefore necessary to measure the OCT data geometry before performing any geometric measurements.

The geometric calibration is performed in two steps. The first step seeks the Cartesian system that best matches the data set. The second step aims at measuring the volume distortion from the perfect grid found in the first step.

The first step uses the overall shape of the well obtained by the OCT 3-D acquisition to find the pixel-to-micrometer scale ratio that fits the theoretical shape of the well. The

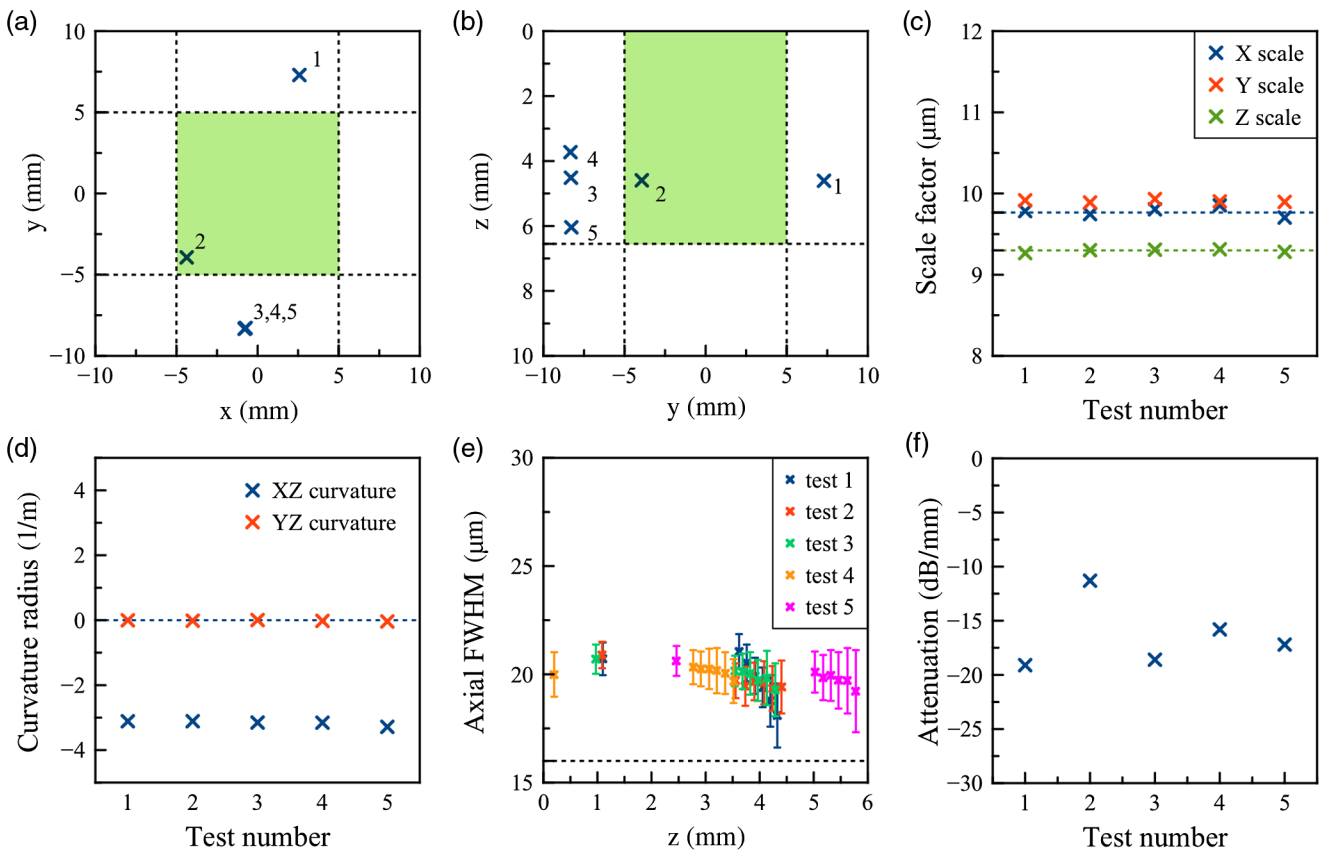

Fig. 6 (a and b) Position of the center of the deepest well step center in the (a) *xy*-plane and (b) *yz*-plane. The imaged region is in green. The numbers correspond to the test number. (c) Measured scale factor in each dimension. The blue and green dashed lines are the system specifications for the *x*- (and *y*-) axis and for the *z*-axis, respectively. (d) Measured curvature of the first interface (air-phantom). The dashed line represents a perfectly telecentric system. (e) Mean and standard deviation of the axial response FWHM for each well step and the first interface as function of depth. The black dashed dot is the system specification. (f) Attenuation slope observed in the mirror step region.

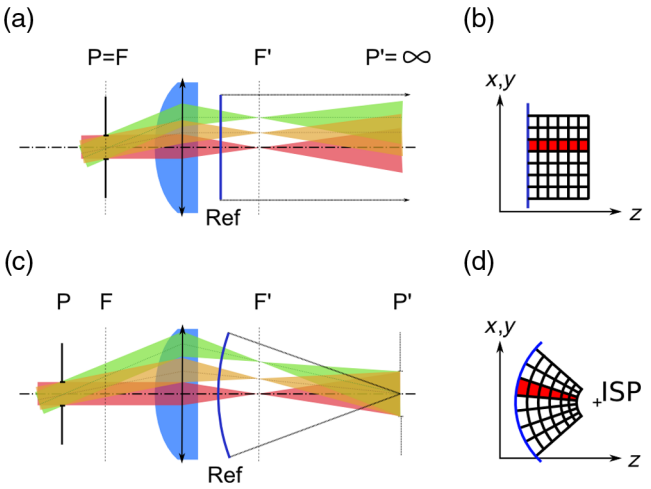

Fig. 7 Illustration of (a) telecentric and (c) nontelecentric scanning mechanisms. P, P', F, and F' are the pupil plan, the image of the pupil plane, and the front and back focal planes, respectively. Ref planes traced in blue illustrate the virtual image of the OCT reference plane. In an object-telecentric setup, the pupil plane and the focal plane are collocated. (b) and (d) The resulting B-scan geometry of (a) and (c), respectively. (x, y, z) is a Cartesian system associated with the laboratory, where z matches the optical system axis. The red-highlighted zone corresponds to a single A-line. ISP (image of the scanning point) is plotted.

measured scale factors for each experiment are presented in Fig. 6(c), as well as the system's specified values. By averaging results from the five tests, x-, y-, and z-axes scale ratio of 9.78 ± 0.06, 9.92 ± 0.03, and 9.29 ± 0.02 μm/pixel are measured, respectively. The 1% error between experiments shows the robustness of the proposed method. Moreover, the results are consistent with the values given by the system specifications (x: 9.77 μm/pixel, y: 9.77 μm/pixel, and z: 9.30 μm/pixel). In the axial dimension, the ratio uncertainty does not only depend on the 3-D fitting error but also on the uncertainty of the refractive index of the phantom material, as OCT measures optical path differences. An additional uncertainty due to refractive index has to be added to the measured z-axis scale, hence a z-scale factor of 9.29 ± 0.13 μm/pixel. Overall, the method provides volume size with 2% accuracy in all axes.

For the second step, the curvature of the air-phantom interface in the acquired volume is measured using a biconical fit that models defocusing. The curvatures for each test in each axis are shown in Fig. 6(d). The mean curvatures are zero in the xz-plane and $3.2 \pm 0.1\text{m}^{-1}$ in the yz-plane. Any curvature is due to an error in the pupil position or to pupil imaging aberrations and could be increased by any nonlinearity of the galvanometer scan. If the pupil position error is considered as the principal source of distortion, the measurement of this curvature is sufficient to correct the whole volume distortion. Indeed, from this curvature, it is possible to deduce the position of the image of the scanning point (ISP), and a spherical-to-Cartesian coordinates transformation can then be used to correct the volume geometry, as shown in Fang et al.[16]

3.2 *Axial Resolution*

The axial resolution is obtained by measuring the FWHM of a signal peak due to the reflection from an interface. Figure 6(e) plots the mean and standard deviation axial response FWHM of each mirror segment for each test as well as for the first interface. The smallest and largest measured FWHM are 18.1 and 21.1 μm, respectively. The maximum standard deviation for all those individual measurements is 2 μm. FHWM decreases with depth within the phantom but not with absolute position with respect to the reference mirror. This suggests that the effect is due to the lower SNR at greater depth as opposed to nonlinear k-space sampling, a mechanism that would otherwise cause the FWHM to increase with distance from the reference plane. Overall, the measured axial FWHM is 20 ± 2 μm independently of the depth where it was measured. To validate our method, the axial response was also measured with the conventional procedure, which relies on scanning a mirror across the axial FOV. The mirror-scanning method yielded an FWHM of 21 ± 1 μm. Both measurements are within 5% of each other, but differ from the specified resolution (16 μm). This may come from variation in the laser spectrum since its purchase. This shows the importance monitoring a system's performance over time.

3.3 *Intensity Response Calibration*

Calibration and benchmarking of OCT system signal intensity are mainly done using two parameters. The first is the system depth-dependent ability to detect a reflector, known as system fall-off or roll-off. The second is the system sensitivity, which corresponds to the reflectance level required to produce an SNR of 1 (or 0 dB).

Fall-off measurements are usually performed by axially translating a mirror. As the mirror reflectivity is constant, any detected signal variation is due to the system. Sensitivity (linear ratio) is obtained by dividing the SNR measured for a known reflector by its reflection coefficient.

The calibration object was first designed to allow measuring sensitivity and roll-off. Indeed, the combined knowledge of the phantom's attenuation coefficient, its thickness above a particular mirror segment, and the absolute reflectivity of each mirror segment should have allowed for sensitivity measurements. Additionally, the multiple mirror segments positioned at increasing depth should have enabled system fall-off measurements. In practice, however, without controlling the tilt of the calibration object, and, moreover, with the system's optics causing distortion, the variation in incidence angle and consecutively in collected specular reflection (with lateral position and in between tests) adds too much uncertainty to obtain an absolute reflectivity measurement.

As shown in Fig. 5(a), collected specular reflection varies by up to 30 dB from the first interface signal intensity. It is also shown in Fig. 6(f), which plots the attenuation slope in the mirror step regions. These values are obtained from the variation of median reflectivity for each step as a function of depth. The attenuation slope ranges from -11 to -19 dB/mm for tests 1 and 2, respectively. Overall, such uncertainties prevent any sensitivity or fall-off characterization and will be addressed in a future iteration.

4 Discussion and Conclusion

The results show that the combination of the high-precision calibration system coupled with tissue phantom, along with the proposed algorithm, succeeds in calibrating the acquisition geometry of an OCT system. It provides the user with the

Cartesian system that best matches the acquired data, and obtains the pixel-to-micrometer scale factor with about 2% uncertainty in all axes. It also provides the user with the FOV curvature, which can be used to correct geometric distortion in the imaged volume. These parameters are usually sufficient to correct geometric measurements performed in most biological applications. In more demanding cases, a complete 3-D distortion map may be required as well as an algorithm that corrects refractions at interfaces. The current calibration object does not allow for such precise 3-D distortion map measurements, as it does not possess calibration points that cover the whole OCT volume. Nevertheless, a modified version of the object, composed of layers of phantom material with different optical properties, could perform such a task.

The method also measures the median system axial response FWHM for all the mirror segments. Being able to compare the axial FWHM response over time allows monitoring any degradation in the image resolution and laser bandwidth. Moreover, by measuring the axial response at several depths, nonlinearity in *k*-space sampling can be assessed. For the moment, lateral resolution cannot be assessed, but in the next version of the object, the transition section between well steps could incorporate vertical edges for this purpose.

In the future, we plan to add intensity measurements to the method to quantitatively measure system sensitivity and signal fall-off. This could be achieved with the characterization of the phantom material attenuation coefficient and by changing the interface reflectance properties. Ideally, the interfaces should have a Lambertian reflectance profile. In this case, the reflected intensity would be the same in every direction and at every position, and the measured signal would be independent of the laser beam incidence angle.

The method presented here can easily and in less than 10 min benchmark an OCT system. Currently, the longest step in the calibration procedure is the time required for saving and loading individual image files after an acquisition. We therefore believe that by using a volumetric file type as input and by improving the algorithm, the duration of the procedure could be reduced to less than 1 min.

The capacity to rapidly calibrate a system is of paramount importance in the development of the field of OCT and of biomedical optics in general. The clumsiness of today's calibration procedures limits the comparison of OCT data, as the precise state of the system used to create them is unknown. We believe that the calibration object combined with its automatic analysis algorithm answers this problem by providing a simple and quick method to characterize an OCT system.

Acknowledgments

This work was supported by the Canada Foundation for Innovation (CFI), the National Science and Engineering Research Council Canada (NSERC), and the Groupe de Recherche en Sciences et Technologies Biomedicales (GRSTB).

References

1. D. Huang et al., "Optical coherence tomography," *Science* **254**(5035), 1178–1181 (1991).
2. M. Wojtkowski et al., "In vivo human retinal imaging by Fourier domain optical coherence tomography," *J. Biomed. Opt.* **7**(3), 457–463 (2002).
3. N. Nassif et al., "In vivo human retinal imaging by ultrahigh-speed spectral domain optical coherence tomography," *Opt. Lett.* **29**(5), 480–482 (2004).
4. I.-K. Jang et al., "Visualization of coronary atherosclerotic plaques in patients using optical coherence tomography: comparison with intravascular ultrasound," *J. Am. Coll. Cardiol.* **39**(4), 604–609 (2002).
5. A. M. Zysk et al., "Optical coherence tomography: a review of clinical development from bench to bedside," *J. Biomed. Opt.* **12**(5), 051403 (2007).
6. G. J. Tearney et al., "Consensus standards for acquisition, measurement, and reporting of intravascular optical coherence tomography studies: a report from the international working group for intravascular optical coherence tomography standardization and validation," *J. Am. Coll. Cardiol.* **59**(12), 1058–1072 (2012).
7. P. H. Tomlins et al., "Femtosecond laser micro-inscription of optical coherence tomography resolution test artifacts," *Biomed. Opt. Express* **2**(5), 1319–1327 (2011).
8. R. Y. Gu et al., "Variable-sized bar targets for characterizing three-dimensional resolution in OCT," *Biomed. Opt. Express* **3**(9), 2317–2325 (2012).
9. A. Curatolo, B. F. Kennedy, and D. D. Sampson, "Structured three-dimensional optical phantom for optical coherence tomography," *Opt. Express* **19**(20), 19480–19485 (2011).
10. J.-P. Bouchard et al., "Accurately characterized optical tissue phantoms: how, why and when?," *Proc. SPIE* **7906**, 79060K (2011).
11. J. Baxi et al., "Retina-simulating phantom for optical coherence tomography," *J. Biomed. Opt.* **19**(2), 021106 (2014).
12. J.-P. Bouchard et al., "Reference optical phantoms for diffuse optical spectroscopy. Part 1—error analysis of a time resolved transmittance characterization method," *Opt. Express* **18**(11), 11495–11507 (2010).
13. K. L. Lurie, B. F. T. Mistree, and A. K. Ellerbee, "CloudOCT: an online data- and code-sharing platform to accelerate research progress," in *Photonics West 2015 BIOS*, Stanford University, pp. 9312–9393.
14. "Automated OCT calibration," 2015, https://cloudoct.com/show_root_folder?folder_id=179 (2 December 2015).
15. J. Schindelin et al., "Fiji: an open-source platform for biological-image analysis," *Nat. Methods* **9**(7), 676–682 (2012).
16. L. Fang et al., "Sparsity based denoising of spectral domain optical coherence tomography images," *Biomed. Opt. Express* **3**(5), 927–942 (2012).

Biographies for the authors are not available.